

## Semiconducting carbon nanotube network thin-film transistors with enhanced inkjet-printed source and drain contact interfaces

Yongwoo Lee, Jinsu Yoon, Bongsik Choi, Heesung Lee, Jinhee Park, Minsu Jeon, Jungmin Han, Jieun Lee, Yeamin Kim, Dae Hwan Kim, Dong Myong Kim, and Sung-Jin Choi

Citation: *Appl. Phys. Lett.* **111**, 173108 (2017);

View online: <https://doi.org/10.1063/1.5009656>

View Table of Contents: <http://aip.scitation.org/toc/apl/111/17>

Published by the [American Institute of Physics](#)

---

---

The banner features a dark blue background with a network of glowing yellow and white nodes connected by thin blue lines, resembling a molecular or data network. The text is positioned on the left side of the banner.

**SciLight**

Sharp, quick summaries **illuminating**  
the latest physics research

Sign up for **FREE!**

**AIP**  
Publishing

## Semiconducting carbon nanotube network thin-film transistors with enhanced inkjet-printed source and drain contact interfaces

Yongwoo Lee, Jinsu Yoon, Bongsik Choi, Heesung Lee, Jinhee Park, Minsu Jeon, Jungmin Han, Jieun Lee, Yeamin Kim, Dae Hwan Kim, Dong Myong Kim, and Sung-Jin Choi<sup>a)</sup>

*School of Electrical Engineering, Kookmin University, Seoul 02707, South Korea*

(Received 25 May 2017; accepted 18 October 2017; published online 27 October 2017)

Carbon nanotubes (CNTs) are emerging materials for semiconducting channels in high-performance thin-film transistor (TFT) technology. However, there are concerns regarding the contact resistance ( $R_{\text{contact}}$ ) in CNT-TFTs, which limits the ultimate performance, especially the CNT-TFTs with the inkjet-printed source/drain (S/D) electrodes. Thus, the contact interfaces comprising the overlap between CNTs and metal S/D electrodes play a particularly dominant role in determining the performances and degree of variability in the CNT-TFTs with inkjet-printed S/D electrodes. In this work, the CNT-TFTs with improved device performance are demonstrated to enhance contact interfaces by controlling the CNT density at the network channel and underneath the inkjet-printed S/D electrodes during the formation of a CNT network channel. The origin of the improved device performance was systematically investigated by extracting  $R_{\text{contact}}$  in the CNT-TFTs with the enhanced contact interfaces by depositing a high density of CNTs underneath the S/D electrodes, resulting in a 59% reduction in  $R_{\text{contact}}$ ; hence, the key performance metrics were correspondingly improved without sacrificing any other device metrics. *Published by AIP Publishing.*

<https://doi.org/10.1063/1.5009656>

Carbon nanotubes (CNTs) have recently emerged as prospective materials to provide high carrier mobility<sup>1–3</sup> and excellent thermal conductivity,<sup>4,5</sup> mechanical flexibility,<sup>6,7</sup> and chemical stability,<sup>8,9</sup> as well as high strength.<sup>10,11</sup> Due to these superior material properties, CNTs have therefore been used as semiconducting channels especially for high-performance thin-film transistor (TFT) applications in analog and digital circuits and display backplanes.<sup>12–14</sup> Nevertheless, CNT-TFTs based on percolative CNT network channels still have limitations for modulating on/off states due to the coexistence of both metallic and semiconducting CNTs in the network channel.<sup>2,15–17</sup> The unwanted metallic CNTs in the channel result in a low on/off current ratio for single device operation and high static power consumption in logic circuit operation. Thus, there have been tremendous advances in obtaining high-purity semiconducting CNTs through the solution process that allows CNTs to be rapidly and cheaply separated according to their electronics types, i.e., semiconducting and metallic CNTs.<sup>18,19</sup> Therefore, TFTs with record-breaking performance have been demonstrated using CNTs achieved from a density-gradient ultracentrifugation method with semiconducting purity above 99%.<sup>20,21</sup>

One of the most promising aspects of CNT-TFTs is their compatibility with low-cost, high-throughput printing processes. Inkjet printing is a very common and easily accessible method for the fabrication of CNT-TFTs; hence, various CNT-TFTs and their integrated circuits have been actively demonstrated using the inkjet printing method.<sup>6,22,23</sup> However, worse electrical properties have been reported in the CNT-TFTs, especially with the inkjet-printed source/drain (S/D) contacts, such as low carrier mobility and high operating voltage,

originating from the non-uniform morphology of the printed S/D layers and the resulting substantial contact resistance ( $R_{\text{contact}}$ ) than in the CNT-TFTs with evaporated S/D contacts. Of interest,  $R_{\text{contact}}$  in CNT-TFTs comprised of the overlap between semiconducting CNTs and metal S/D electrodes plays a particularly dominant role in determining the performances and degree of variability in CNT-TFTs, even with a long channel length.<sup>24,25</sup> Therefore, it is necessary to further improve the electrical properties of the CNT-TFTs by optimizing the contact interface.

The present work demonstrates the CNT-TFTs with enhanced inkjet-printed S/D contact interfaces for better device performance. For the enhanced contact interfaces, the density of CNTs underneath the S/D electrodes was controlled during CNT network formation. That is, a higher CNT density was utilized for the region underneath the S/D electrodes, but a lower CNT density was used to reduce the probability of a metallic interconnection between the S/D electrodes for enhanced on/off current ratios.<sup>14–17</sup>  $R_{\text{contact}}$  was systematically investigated for different contact configurations in the CNT-TFTs with the inkjet-printed S/D electrodes to uncover the causes of improved device performance. The results revealed that a high CNT density underneath the S/D electrodes can enhance the contact interfaces by increasing the contact area between the CNT thin film and the S/D electrodes; hence, a 59% decrease in  $R_{\text{contact}}$  was obtained, and the electrical performance was correspondingly improved, such as on-state current ( $I_{\text{ON}}$ ), transconductance ( $g_m$ ), and carrier mobility ( $\mu_{\text{FE}}$ ). Therefore, this work can provide an efficient method for improving the CNT-TFT performance without sacrificing any other device metrics.

Figure 1 illustrates the details of the fabrication processes of the CNT-TFTs with the enhanced inkjet-printed S/D

<sup>a)</sup>Electronic mail: sjchoiee@kookmin.ac.kr. Tel.: +82-2-910-5543.

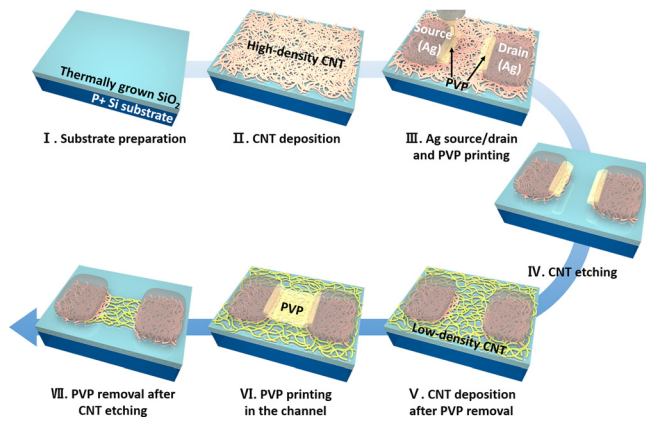


FIG. 1. Process flow of the CNT-TFT with enhanced inkjet-printed S/D contact interfaces. (I) Preparing silicon wafer by first cleaning; (II) CNT deposition with a high density of CNTs for increasing the overlap area between semiconducting CNTs and S/D electrodes; (III) Ag printing at the S/D electrodes and PVP printing at both ends of the channel region; (IV) CNT etching using oxygen plasma; (V) PVP removal and CNT deposition with a lower density for the formation of the CNT network channel; (VI) PVP printing to define the exact channel width; and (VII) CNT etching using oxygen plasma to remove unwanted CNTs, followed by PVP removal.

contact interfaces using a high CNT density underneath the S/D electrodes. Highly purified, pre-separated, 99% semiconducting CNTs were utilized for the formation of the percolated network. First, CNT-TFT fabrication was started on the silicon substrate, which was highly p-doped to serve as the global back gate, with a thermally grown 55-nm-thick silicon dioxide ( $\text{SiO}_2$ ) layer. Next, the substrate was cleaned by oxygen plasma treatment (30 W) for 1 min and was then functionalized with a poly-L-lysine solution (0.1% w/v in  $\text{H}_2\text{O}$ ; Sigma Aldrich) by dropping the solution onto the  $\text{SiO}_2$  surface to introduce an amine-terminated adhesion layer for the deposition of the semiconducting CNTs. The poly-L-lysine solution is biocompatible with the CNTs and has a plentiful active amino group; hence, the effective adhesion layer was formed on the  $\text{SiO}_2$  surface.<sup>6,9,12–14,26–30</sup> The substrate was thoroughly rinsed with deionized (DI) water and dried with flowing nitrogen gases. After that, to form the CNT networks, the substrate was immersed in the CNT solution with high semiconducting purity (99%) (IsoNanotubes-S<sup>TM</sup>, provided from NanoIntegrus, Inc.) for 18 h. Note that for the enhanced contact interfaces caused by the large overlap area between semiconducting CNTs and metal S/D electrodes, a high density of CNTs was selected for underneath the S/D electrodes but not in the channel region by keeping a relatively low CNT density. To form the S/D electrodes, a silver (Ag) nanoparticle ink (Tec-IJ-060, InkTec) was printed using a commercial inkjet printer (Unijet UJ200MF) after the substrate was rinsed by DI water and isopropanol. Thereafter, the printed S/D electrodes were sintered at 150 °C for 10 min to merge the particles for the reduced resistance. Next, poly-4-vinylphenol (PVP, Sigma Aldrich) was printed only at both ends of the channel region by marginally overlapping with the printed S/D electrodes, followed by through annealing at 80 °C for 30 min to harden PVP. Then, the CNTs were removed by an oxygen plasma-etching step (80 W) for 3 min, except for the areas where PVP and S/D electrodes were printed, followed by thorough removal of the printed PVP with acetone at 70 °C

for 1 h, isopropanol, and flowing nitrogen sequentially. Then, the substrate was again immersed in the same 99% semiconducting CNT solution during 13 h for the formation of the CNT network channel comprised of a low CNT density and rinsed with DI water and isopropanol. Note that the percolated network composed of semiconducting CNTs was only formed on the  $\text{SiO}_2$  substrate, not on the Ag S/D electrodes because the CNTs were selectively deposited on the amine-terminated  $\text{SiO}_2$  surface. PVP was also printed again to define the channel width, followed by one more oxygen plasma-etching step to remove unwanted CNT paths outside the channel region. PVP was also printed again to define the channel width, followed by one more oxygen plasma-etching step to remove unwanted CNT paths outside the channel region. Finally, PVP was removed using acetone, isopropanol, and flowing nitrogen.

Figure 2(a) presents a schematic illustration of the CNT-TFTs with enhanced inkjet-printed S/D contact interfaces. Note that the CNT densities were controlled for the regions at the network channel and underneath the S/D electrodes. A high density of CNTs underneath the S/D electrodes produced from a deposition time of 18 h is expected to enhance the contact interfaces by increasing the overlap between the semiconducting CNTs and S/D electrodes, resulting in the lowered  $R_{\text{contact}}$ . In addition, it is expected that a low CNT density in the network channel produced from a deposition time of 13 h would result in a higher on/off current ratio by reducing the probability of the percolative transport through metallic CNTs. Figure 2(b) depicts the optical image of the global back gate CNT-TFT with the printed Ag S/D electrodes. The CNT network channel defined by  $\text{O}_2$  plasma has an approximate width ( $W$ ) of  $400 \mu\text{m} \pm 25 \mu\text{m}$  and a channel length ( $L$ ) of  $250 \mu\text{m} \pm 25 \mu\text{m}$ . Figure 2(c) shows atomic force microscopy (AFM) images of the percolative CNT network constructed from the 99% semiconducting CNTs. In the AFM images, it was clearly confirmed that the CNT density underneath the S/D electrodes was higher than at the network

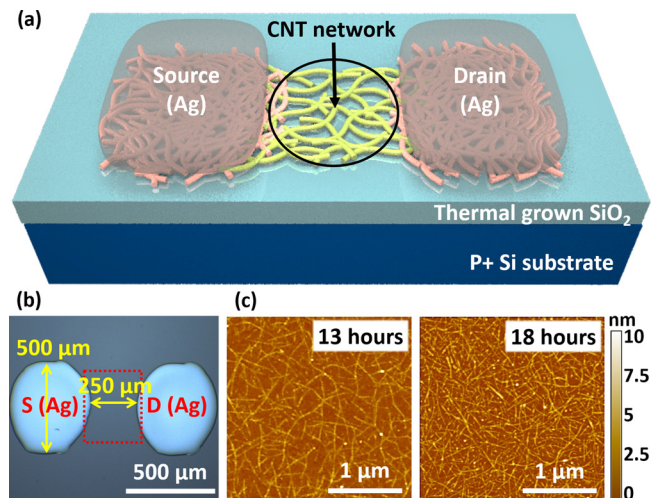


FIG. 2. (a) Schematic illustration of the CNT-TFT with enhanced inkjet-printed S/D contact interfaces. (b) Optical microscopy image of the fabricated CNT-TFT with inkjet-printed S/D electrodes. (c) AFM images ( $2.5 \times 2.5 \mu\text{m}$ , the z-scale is 10 nm) of the CNT network channel constructed from a 99% semiconducting CNT solution with deposition times of 13 h and 18 h.

channel. The average CNT densities formed at each deposition time were carefully calculated manually as  $70 \pm 5$  and  $98 \pm 2$  tubes/ $\mu\text{m}^2$  for 13 and 18 h, respectively. Importantly, the AFM images also confirmed that the standard CNT density deviation was evidently reduced with a longer deposition time. This would be expected to greatly improve the uniformity of the contact interfaces in the CNT-TFTs.

The transfer characteristics (i.e., drain current,  $I_{DS}$  vs. gate voltage,  $V_{GS}$ ) of the representative CNT-TFTs with the enhanced contact interfaces at a drain voltage ( $V_{DS}$ ) of  $-0.5$  V are shown in Fig. 3(a). The control CNT-TFTs, i.e., conventional CNT-TFTs, in which the CNT densities were identical through all regions in the channel and underneath the S/D electrodes, were also compared. Interestingly, the CNT densities were exactly the same, i.e., the network channels in two devices were produced from the same deposition time of 13 h; overall, device performances were enhanced for the CNT-TFTs with a longer deposition time of 18 h underneath the S/D electrodes without any sacrifices compared with CNT-TFTs with a shorter deposition time of 13 h. Most representatively, 99% improved on-state current was obtained, which is mostly attributed to the enhanced contact interfaces. The output characteristics (i.e.,  $I_{DS}$  vs.  $V_{DS}$ ) of the CNT-TFTs with and without the enhanced contact interfaces are shown in Fig. 3(b). Importantly, the output characteristic curves appeared to be linear at small  $V_{DS}$  values, indicating that ohmic contact was well formed between the Ag S/D electrodes and CNT networks, regardless of the contact configuration. The  $V_{DS}$  value was negatively increased, while  $I_{DS}$  became a constant value, that is, the device exhibited the saturation behavior, indicating the reasonable field-effect operation.

There was a slight threshold voltage ( $V_T$ ) variation in CNT-TFTs with different CNT densities underneath the S/D electrodes.  $V_T$  was extracted using a linear extrapolation method as approximately  $-20$  V  $\pm$  0.15 V for the control CNT-TFTs, but the CNT-TFT with the enhanced contact interfaces showed a  $V_T$  value of  $-19.75$  V  $\pm$  0.18 V. Therefore, the device performances were compared based on the overdrive voltage, i.e.,  $V_{OV} = V_{GS} - V_T$ , for a fair comparison. The key

metrics of the devices, such as normalized on-state current ( $I_{ON}$ ), i.e.,  $-I_{ON} \times L/W$  ( $I_{ON}$  is defined at  $V_{OV} = -5$  V and  $V_{DS} = -0.5$  V), on/off current ratio, i.e.,  $\log(I_{ON}/I_{OFF})$  (the off-state current,  $I_{OFF}$ , is defined at  $V_{OV} = 10$  V and  $V_{DS} = -0.5$  V), normalized transconductance ( $g_m$ ), i.e.,  $g_m \times L/W$ , and carrier mobility ( $\mu_{FE}$ ) were compared in Fig. 3(c). For the extraction of  $\mu_{FE}$ , the following equation was used:

$$\mu_{FE} = \frac{L}{W} \frac{1}{C_G V_{DS}} \frac{\partial I_{DS}}{\partial V_{GS}} = \frac{L}{W} \frac{g_m}{C_G V_{DS}}, \quad (1)$$

where  $C_G$  is the gate capacitance per unit area. The gate capacitance was also calculated by using a sophisticated cylindrical model,<sup>31</sup> as shown in the following equation:

$$C_G = \left\{ C_Q^{-1} + \frac{1}{2\pi\epsilon_0\epsilon_{ox}} \ln \left[ \frac{\Lambda_0 \sinh(2\pi t_{ox}/\Lambda_0)}{R} \right] \right\}^{-1} \Lambda_0^{-1}, \quad (2)$$

where  $\Lambda_0^{-1}$  stands for the density of the CNTs,  $C_Q$  is the quantum capacitance ( $4.0 \times 10^{-10}$  F/m),  $R$  is the average radius of the CNTs (in our case, 0.7 nm),  $\epsilon_{ox}$  is the dielectric constant of  $\text{SiO}_2$  (3.9), and  $\epsilon_0$  is the permittivity in vacuum ( $8.854 \times 10^{-12}$  F/m). The off-state of the representative devices was essentially consistent without any significant variations. The on-state, however, was shown to change substantially between different contact configurations. The on-state currents for CNT-TFTs with the enhanced contacts were much larger, i.e., 96% increased normalized  $I_{ON}$ , compared with the conventional CNT-TFTs, which is evidence for the dominant role that contact interfaces play in determining the performance of CNT-TFTs. In addition, other key metrics of the device performance exhibited a similar enhancement, indicating improved overall device performances for CNT-TFTs with enhanced contact interfaces resulting from a high CNT density underneath the S/D electrodes.

Different contact configurations were also compared by extracting  $R_{contact}$  using the transmission line method (TLM)<sup>32,33</sup> for CNT-TFTs different  $L$  values ranging from 150  $\mu\text{m}$  to 350  $\mu\text{m}$ . As given in Fig. 4(a), the total resistance ( $R_{total}$ ) of CNT-TFTs with the enhanced contact interfaces

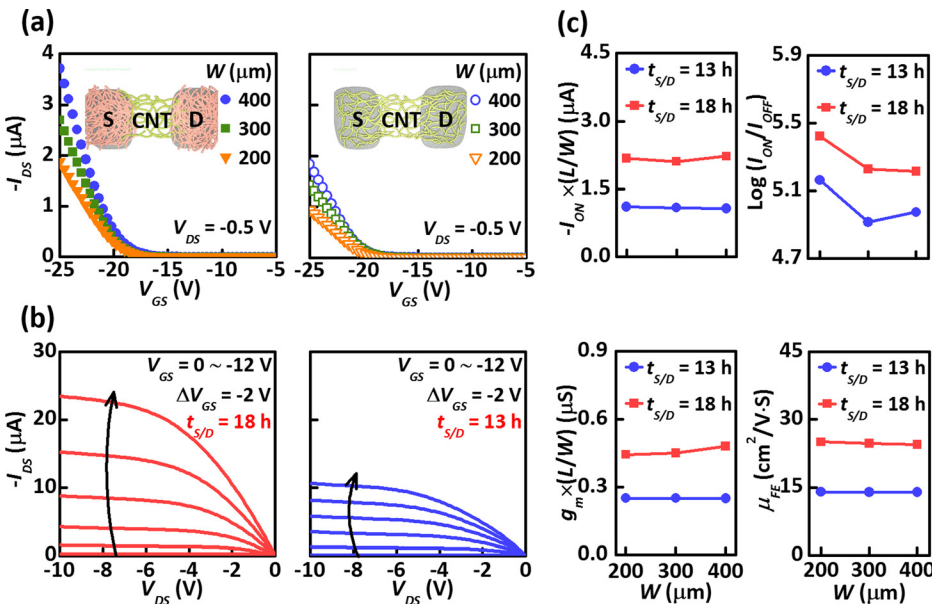


FIG. 3. (a) Transfer characteristics ( $I_{DS}$ - $V_{GS}$ ) and (b) output characteristics ( $I_{DS}$ - $V_{DS}$ ) of the CNT-TFTs ( $L = 250$   $\mu\text{m}$ ) with different CNT densities underneath the S/D electrodes and with the same density of CNTs at the channel.  $t_{S/D}$  indicates the deposition times of CNTs in the region underneath the S/D electrodes. The CNT deposition times for the network channel formation were equal to 13 h. (c) Normalized on-state current ( $I_{ON}$ ),  $\log(I_{ON}/I_{OFF})$ , normalized transconductance ( $g_m$ ), and carrier mobility ( $\mu_{FE}$ ) for the CNT-TFTs with different CNT densities underneath the S/D electrodes.

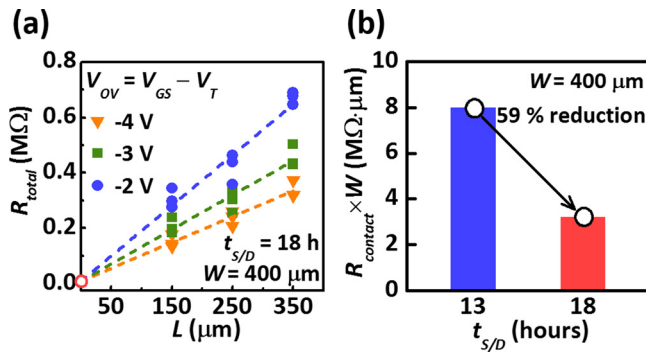


FIG. 4. (a) Representative TLM plot of the  $R_{total}$  of the CNT-TFTs with enhanced contact interfaces as a function of  $L$  at overdrive voltages ( $V_{OV} = -4$  V,  $-3$  V, and  $-2$  V). (b) Normalized  $R_{contact}$  for the CNT-TFTs with different densities of CNTs underneath the S/D electrodes.

was plotted as a function of  $L$  for different  $V_{OV}$  values of  $-2$  V,  $-3$  V, and  $-4$  V.  $R_{total}$  for the devices can be expressed by the following equation:

$$R_{total}(V_{GS}) = \frac{V_{DS}}{I_{DS}} = R_{contact} + R_{ch} = R_{contact} + L \times r_{ch}, \quad (3)$$

where  $R_{ch}$  is the device channel resistance and  $r_{ch}$  is a  $V_{GS}$ -dependent channel resistivity. Therefore,  $R_{contact}$  between semiconducting CNTs and S/D metal electrodes could be extracted from the intercept of the linear fit to the TLM plot. The normalized  $R_{contact}$  with respect to  $W$  (i.e.,  $R_{contact} \times W$ ) for CNT-TFTs with and without the enhanced contact interfaces was extracted as approximately 3.2  $M\Omega \cdot \mu m$  and 8.0  $M\Omega \cdot \mu m$ , respectively, as shown in Fig. 4(b). That is, CNT-TFTs with a higher CNT density underneath the S/D electrode reduced  $R_{contact}$  by 59%, compared to the conventional CNT-TFTs.

In conclusion, the facile method was demonstrated to improve the performance of CNT-TFTs with the inkjet-printed S/D electrodes by controlling the CNT density underneath the S/D electrodes. A higher CNT density was utilized underneath the S/D metal electrodes to increase the contact area for improving the contact interfaces. On the other hand, the CNT density at the network channel was lowered to decrease the probability of a metallic interconnection between the S/D electrodes. As a result,  $R_{contact}$  was reduced by 59%, thereby improving the key performance metrics, such as  $I_{ON}$ ,  $I_{ON}/I_{OFF}$ ,  $g_m$ , and  $\mu_{FE}$ . Therefore, these findings for the contact configuration can provide an easy method for improving CNT-TFT performance and guide further development of printed nanomaterial electronics.

This work was supported by the National Research Foundation (NRF) to Korea under Grant Nos. 2016R1A2B4011366 and 2016R1A5A1012966 and partially by the Future Semiconductor Device Technology Development Program (Grant No. 10067739) funded by MOTIE (Ministry of Trade, Industry & Energy) and KSRC (Korea Semiconductor Research Consortium).

- <sup>1</sup>T. Dürkop, S. A. Getty, E. Cobas, and M. S. Fuhrer, *Nano Lett.* **4**, 35 (2004).
- <sup>2</sup>E. S. Snow, P. M. Campbell, M. G. Ancona, and J. P. Novak, *Appl. Phys. Lett.* **86**, 033105 (2005).
- <sup>3</sup>X. Cao, F. Wu, C. Lau, Y. Liu, Q. Liu, and C. Zhou, *ACS Nano* **11**, 2008 (2017).
- <sup>4</sup>E. Pop, D. Mann, Q. Wang, K. Goodson, and H. Dai, *Nano Lett.* **6**, 96 (2006).
- <sup>5</sup>T. S. Gspann, S. M. Juckes, J. F. Niven, M. B. Johnson, J. A. Elliott, M. A. White, and A. H. Windle, *Carbon* **114**, 160 (2017).
- <sup>6</sup>L. Cai, S. Zhang, J. Miao, Z. Yu, and C. Wang, *ACS Nano* **10**, 11459 (2016).
- <sup>7</sup>P. H. Lau, K. Takeki, C. Wang, Y. Ju, J. Kim, Z. Yu, T. Takahashi, G. Cho, and A. Javey, *Nano Lett.* **13**, 3864 (2013).
- <sup>8</sup>D. Shahrjerdi, A. D. Franklin, S. Oida, J. A. Ott, G. S. Tulevski, and W. Haensch, *ACS Nano* **7**, 8303 (2013).
- <sup>9</sup>S. Zhang, L. Cai, T. Wang, R. Shi, J. Miao, L. Wei, Y. Chen, N. Sepúlveda, and C. Wang, *Sci. Rep.* **5**, 17883 (2015).
- <sup>10</sup>T. Yamada, Y. Hayamizu, Y. Yamamoto, Y. Yomogida, A. Izadi-Najafabadi, D. N. Futaba, and K. Hata, *Nat. Nanotechnol.* **6**, 296 (2011).
- <sup>11</sup>L. Cai, L. Song, P. Luan, Q. Zhang, N. Zhang, Q. Gao, D. Zhao, X. Zhang, M. Tu, F. Yang, W. Zhou, Q. Fan, J. Luo, W. Zhou, P. M. Ajayan, and S. Xie, *Sci. Rep.* **3**, 3048 (2013).
- <sup>12</sup>C. Wang, J.-C. Chien, K. Takeki, T. Takahashi, J. Nah, A. M. Niknejad, and A. Javey, *Nano Lett.* **12**, 1527 (2012).
- <sup>13</sup>J. Zhang, C. Wang, and C. Zhou, *ACS Nano* **6**, 7412 (2012).
- <sup>14</sup>C. Wang, J. Zhang, K. Ryu, A. Badmaev, L. G. De Arco, and C. Zhou, *Nano Lett.* **9**, 4285 (2009).
- <sup>15</sup>D. Lee, M.-L. Seol, D.-I. Moon, P. Bennett, N. Yoder, J. Humes, J. Bokor, Y.-K. Choi, and S.-J. Choi, *Appl. Phys. Lett.* **104**, 143508 (2014).
- <sup>16</sup>S.-J. Choi, C. Wang, C. C. Lo, P. Bennett, A. Javey, and J. Bokor, *Appl. Phys. Lett.* **101**, 112104 (2012).
- <sup>17</sup>S.-J. Choi, P. Bennett, D. Lee, and J. Bokor, *Nano Res.* **8**, 1320 (2015).
- <sup>18</sup>M. S. Arnold, A. A. Green, J. F. Hulvat, S. I. Stupp, and M. C. Hersam, *Nat. Nanotechnol.* **1**, 60 (2006).
- <sup>19</sup>M. S. Arnold, S. I. Stupp, and M. C. Hersam, *Nano Lett.* **5**, 713 (2005).
- <sup>20</sup>G. S. Tulevski, A. D. Franklin, D. Frank, J. M. Lobe, Q. Cao, H. Park, A. Afzali, S.-J. Han, J. B. Hannon, and W. Haensch, *ACS Nano* **8**, 8730 (2014).
- <sup>21</sup>C. Qiu, Z. Zhang, M. Xiao, Y. Yang, D. Zhong, and L.-M. Peng, *Science* **355**, 271 (2017).
- <sup>22</sup>D. Lee, J. Yoon, J. Lee, B.-H. Lee, M.-L. Seol, H. Bae, S.-B. Jeon, H. Seong, S. G. Im, S.-J. Choi, and Y.-K. Choi, *Sci. Rep.* **6**, 26121 (2016).
- <sup>23</sup>J. Lee, J. Yoon, B. Choi, D. Lee, D. M. Kim, D. H. Kim, Y.-K. Choi, and S.-J. Choi, *Appl. Phys. Lett.* **109**, 263103 (2016).
- <sup>24</sup>C. Cao, J. B. Andrews, A. Kumar, and A. D. Franklin, *ACS Nano* **10**, 5221 (2016).
- <sup>25</sup>A. D. Franklin, D. B. Farmer, and W. Haensch, *ACS Nano* **8**, 7333 (2014).
- <sup>26</sup>J. Liu, M. J. Casavant, M. Cox, D. A. Walters, P. Boul, W. Lu, A. J. Rimberg, K. A. Smith, D. T. Colbert, and R. E. Smalley, *Chem. Phys. Lett.* **303**, 125 (1999).
- <sup>27</sup>T. P. Burgin, J. C. Lewenstein, and D. Werho, *Langmuir* **21**, 6596 (2005).
- <sup>28</sup>M. C. LeMieux, M. Roberts, S. Barman, Y. W. Jin, J. M. Kim, and Z. Bao, *Science* **321**, 101 (2008).
- <sup>29</sup>J. P. Opatkiewicz, M. C. LeMieux, and Z. Bao, *ACS Nano* **4**, 1167 (2010).
- <sup>30</sup>J. Zhang, Y. Fu, C. Wang, P.-C. Chen, Z. Liu, W. Wei, C. Wu, M. E. Thompson, and C. Zhou, *Nano Lett.* **11**, 4852 (2011).
- <sup>31</sup>Q. Cao, M. Xia, C. Kocabas, M. Shim, J. A. Rogers, and S. V. Rotkin, *Appl. Phys. Lett.* **90**, 023516 (2007).
- <sup>32</sup>F. Ante, D. Kälblein, T. Zaki, U. Zschieschang, K. Takimiya, M. Ikeda, T. Sekitani, T. Someya, J. N. Burghartz, K. Kern, and H. Klauk, *Small* **8**, 73 (2012).
- <sup>33</sup>F. Ante, D. Kälblein, U. Zschieschang, T. W. Canzler, A. Werner, K. Takimiya, M. Ikeda, T. Sekitani, T. Someya, and H. Klauk, *Small* **7**, 1186 (2011).